RSC Advances

PAPER

View Article Online
View Journal | View Issue

Cite this: *RSC Adv.*, 2021, **11**, 8282

Structure and photoluminescence of Eu^{3+} doped Sr_2InTaO_6 red phosphor with high color purity†

Jingfen Zhao,[a] Hui Gao,[a] Hui Xu,[a] Zhiwei Zhao,[b] Hongxia Bu,[a] Xuefei Cao,[a] Lining He,[a] Zaifa Yang *[a] and Jiayue Sun[c]

The Eu^{3+}-doped Sr_2InTaO_6 phosphors were obtained by solid-state reaction method and the phase purity of Sr_2InTaO_6:Eu^{3+} samples were investigated by the XRD patterns. The Rietveld refinements were conducted to further obtain crystal structure information and the results indicate Sr_2InTaO_6:Eu^{3+} samples crystallized in the monoclinic system with a P_{121} space group. The optical band gap of Sr_2InTaO_6 was calculated to be 3.84 eV by the diffuse reflectance spectra, which are consistent with the result (3.823 eV) of density functional theory. Under 396 nm excitation, the Sr_2InTaO_6:Eu^{3+} phosphor showed a red photoluminescence band centered at about 624 nm due to the $^5D_0 \rightarrow {}^7F_2$ transition. Monitored at 624 nm, the phosphors showed two wide bands from 200 nm to 500 nm, which originated from the charge-transfer band of Eu^{3+}–O^{2-} and f–f transitions of Eu^{3+} ions. The optimum luminous concentration is 0.12 because of the concentration quenching determined to be a quadrupole–quadrupole interaction. The luminescence decay lifetimes of the Sr_2InTaO_6:Eu^{3+} phosphors were milliseconds. Significantly, the temperature-dependent emission spectra of Sr_2InTaO_6:0.12Eu^{3+} phosphors exhibited good thermal stability and the CIE chromaticity coordinates of Sr_2InTaO_6:0.12Eu^{3+} were (0.6265, 0.3693) with high color purity. The present work demonstrated that the Sr_2InTaO_6:Eu^{3+} red-emitting phosphors show great application in lighting technology.

Received 8th January 2021
Accepted 6th February 2021

DOI: 10.1039/d1ra00165e

rsc.li/rsc-advances

1. Introduction

With the rapid advancement of contemporary society, sustainable development of energy and environmental issues has increasingly attracted extensive attention and become a significant matter for nowadays society. As is known to all, in human's daily work and life, the demand for lighting power is a very great percentage in the total power consumption. But the already invented traditional fluorescent and incandescent lamps have many shortcomings, for instance, high power consumption, short service lifespan, low energy conversion efficiency and environmental pollution, which are inconsistent with the purpose of power economy and environmental protection under the present circumstances.[1–3] Over the years, luminescent materials doped with the rare-earth ions have attracted extensive attention, which has a wide range of applications in many fields especially such as a solid-state lighting system, medical treatment diagnosis, biological imaging, fiber amplifiers, solar cells, light-emitting diodes (LEDs) and so on.[4–7] As a new type of solid luminescent material, white LEDs (WLEDs) have been proverbially put into use in various lighting devices on account of their superior luminescent features, such as, high fluorescent efficiency, energy conservation, light weight, long service lifetime, low heat and environmental friendliness.[8,9] WLEDs are gradually replacing the traditional incandescent lamps as the next generation solid-state optical source.

Up to now, the most common form of exploiting WLEDs is the combination of blue LED chip coated with YAG:Ce^{3+} yellow fluorescent powder.[10,11] Moreover, another way is by combining the ultraviolet (UV) chip or near-ultraviolet (NUV) chip with three basic colors of red, blue, and green (RGB) emitting materials to generate white light.[12,13] While whereby, owing to the lack of efficient red emitting components, the white light would encounter low color rendering index (CRI) and high color temperature.[14] Thus, it is of great significance to research the red-emitting phosphor with good spectral characteristics as novel, stable and high quantum efficiency. Until recently, red light emitting materials *via* doping rare-earth ions (Eu^{3+}, La^{3+}, Ce^{3+}, Tb^{3+}) and transition-metal ions (Mn^{4+}, Cr^{3+}, Pr^{3+}) have aroused extensive attention on the basis of their potential applications in lighting and displays.[15–17] Notably, trivalent rare-earth europium ions (Eu^{3+}) is considered as an important red fluorescent activator which shows outstanding red emission ranging from 605 nm to 630 nm and higher quantum efficiency,

[a]College of Physics and Electronic Engineering, Qilu Normal University, Jinan, 250200, PR China. E-mail: fazaiyang@163.com; Fax: +86 1066778147; Tel: +86 1066778147
[b]College of Automobile and Electronic Engineering, Baoding University, Baoding, 071000, PR China
[c]School of Science, Beijing Technology and Business University, Beijing, 100048, PR China

† Electronic supplementary information (ESI) available. See DOI: 10.1039/d1ra00165e

corresponding to the $^5D_0$–$^7F_2$ transition.[18–20] Further exploration, the Eu^{3+} ions reveal pure magnetic and electric dipole transitions, which is the reason why it is a sensitive probe for the rare-earth ion site structure. As one kind of crucial light source, Eu^{3+} ion has been extensively studied in inorganic solid luminescence field, such as commercially available red-emitting phosphors YVO_4:Eu^{3+}, Y_2O_2S:Eu^{3+}, Y_2O_3:Eu^{3+}, as well as mainly reported materials $LaAlGe_2O_7$:Eu^{3+}, $SrGe_4O_9$:Eu^{3+}, Mg_4GeO_6:Eu^{3+}, Ba_2GeO_4:Eu^{3+}, $Sr_3La_2(Ge_3O_9)_2$:Eu^{3+}, $Na_4Y_2Ge_4O_{13}$:Eu^{3+} and so on.[21–26] Until recently, the excellent performance of Eu^{3+}-doped Sr_2InTaO_6 double perovskite red phosphors under UV or NUV excitation region has not been reported in the current study.

Hereby, we chose the double perovskite oxide Sr_2InTaO_6 as the host material in the present research. A cluster of Eu^{3+}-doped red-emitting fluorescent powders were carefully depicted in this topic. Subsequently, the phase purity and crystal structure were studied by X-ray diffraction (XRD) and scanning electron microscope (SEM). In addition, the photoluminescence excitation (PLE), photoluminescence (PL), lifetime and temperature-dependent photoluminescence were systematically discussed. These results indicate that the synthesized sample Sr_2InTaO_6:Eu^{3+} in this paper is a potential red light emitting phosphor for applications of WLEDs.

2. Experimental section

2.1 Materials and syntheses

The Sr_2InTaO_6:xEu^{3+} (x = 0.04, 0.08, 0.12, 0.16, 0.20, 0.24) samples were fabricated *via* traditional high temperature solid state method. The Eu_2O_3 (99.99%), In_2O_3 (99.9%), Ta_2O_5 (99.5%) and $SrCO_3$ (99.5%) are the raw materials. They are transferred to the crucible to pre-sinter at 600 °C for 6 h after weighting by a certain ratio relating to stoichiometry and mixing uniformly. Then the obtained samples were reground to further burn at 1300 °C for 6 h. Finally, the harvest Sr_2InTaO_6:Eu^{3+} samples were obtained to make further characterization and discussion.

2.2 Characterization

The XRD (D8 Advance, Bruker) was used to identify crystal structures of the sample by using Cu-Kα (λ = 0.15406 Å) radiation. The elementary compositions and morphology were measured by SEM (S-4800, Hitachi). Diffuse reflection spectra (DRS) were detected by the UV-Vis-NIR spectrophotometer (UH4150, Hitachi). The PL, PLE, temperature-dependent emission spectra and decay curves were precisely tested by the fluorescence spectrometer (JOBIN YVON FLuoroLog-3, HORIBA). The first principle calculation was executed by the Cambridge Sequential Total Energy Package (CASTEP) code.

3. Results and discussion

3.1 Crystal structures and phase analysis

The phase purity of Sr_2InTaO_6:Eu^{3+} samples were investigated by the XRD patterns. In Fig. 1, we presented the date of

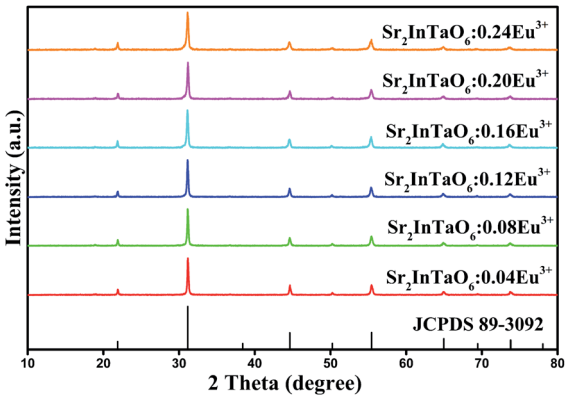

Fig. 1 XRD patterns of Sr_2InTaO_6:xEu^{3+} phosphors (x = 0.04, 0.08, 0.12, 0.16, 0.20, and 0.24) and the standard pattern for Sr_2InTaO_6 (JCPDS No. 89-3092).

Sr_2InTaO_6:xEu^{3+} (x = 0.04, 0.08, 0.12, 0.16, 0.20, and 0.24) with a set of different Eu^{3+}-doped concentrations in the 2θ range of 10°–80°. The detected diffraction peaks from the sample patterns exhibit similar shape and are in good agreement with the Joint Committee on Powder Diffraction Standard (JCPDS) card (No. 89-3092), even the concentration of Eu^{3+} is up to 0.24. This indicates the introduction of Eu^{3+} ions without influence the crystal structure and a pure phase is obtained for the synthesized material. With increasing Eu^{3+} doping concentration, the positions of the diffraction peaks are consistent with

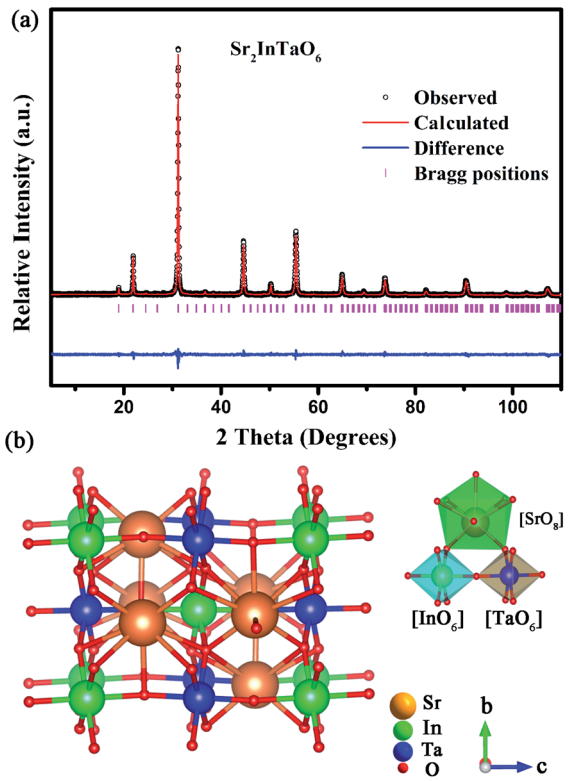

Fig. 2 (a) Rietveld refinement of Sr_2InTaO_6 host, (b) crystal structure of Sr_2InTaO_6.

each other, which also illustrate Eu^{3+} ions have been successfully incorporated into this structure. When introducing Eu^{3+} into the Sr_2InTaO_6 host, the Eu^{3+} ions are be prior substitute for the In^{3+} ions owing to the similar ionic radii between Eu^{3+} (r = 0.947 Å, CN = 6) ions and In^{3+} (r = 0.800 Å, CN = 6).[27]

In order to obtain more detailed information of crystal structure, the Rietveld refinement of Sr_2InTaO_6 was calculated using the general structure analysis system (GSAS) method and illustrated in Fig. 2(a). The solid red and black lines separately marked the theoretical calculation data and experimental observation pattern. The pink vertical bars refer to the sites of Bragg diffraction, and the blue line at the bottom represents the difference between theoretical and experimental data. In Table 1, more detailed crystal structure parameters of the Sr_2InTaO_6:0.12Eu^{3+} samples are provided and the reliability factors R_{wp}, R_p, χ^2 were stable, which illustrate that the refinement results are reliable.[28] From data analysis and comparison, the refinement results confirmed that the crystal belongs to the monoclinic system with a P_{121} space group and the cell parameters are calculated to be a = 5.74 Å, b = 5.75 Å, c = 8.12 Å, and $\alpha = \gamma = 90°$, $\beta = 89.96°$. Moreover, the crystal structure of host Sr_2InTaO_6 and the around coordination environment of Sr, In and Ta atoms are also shown in Fig. 2(b). As can be seen from the diagram, each Sr atom is surrounded by eight nearest neighbor oxygen atoms, each In (or Ta) atom is surrounded by six oxygen atoms to constitute a distorted octahedron with an In–O bond length 2.112 Å and an Ta–O bond length 2.011 Å. These findings suggest that the sites of In^{3+} can be served as dissymmetric core for the doped ions and In^{3+} can be substituted by Eu^{3+} owing to their similar ionic radius.

More detailed morphological and compositional features of Sr_2InTaO_6:0.12Eu^{3+} were demonstrated through the SEM and the elemental mappings are shown in Fig. 3. It can be found that the phosphor is comprised of many agglomerate and irregular microparticles due to the high temperature reaction. And the size of Sr_2InTaO_6:0.12Eu^{3+} is about several micrometers indicating that these powders can satisfy the requirement of production.[29] In addition, the elemental mapping confirms that these elements (Sr, In, Ta, Eu, and O) are homogeneously distributed, further authenticate that the Sr_2InTaO_6:Eu^{3+} phosphors with uniform composition were successfully synthesized.

Table 1 The crystal data and Rietveld refinement results for the Sr_2InTaO_6 host[a]

Atom	X	Y	Z	Occupancy	Mult.
Sr	0.50000	0.00015	0.25000	1.000	4
In	0.00000	0.00000	0.00000	0.500	2
Ta	0.00000	0.00000	0.50000	0.500	2
O1	0.75023	0.76093	0.05344	1.000	4
O2	0.74587	0.17600	0.01214	1.000	4
O3	0.05325	0.12201	0.23431	1.000	4

[a] Space group: $P121/n1$; a = 5.74 Å, b = 5.75 Å, c = 8.12 Å, V = 268.103 Å^3, $\alpha = \gamma = 90°$, $\beta = 89.96°$, R_{wp} (%) = 12.1, R_p (%) = 8.94, χ^2 = 1.43.

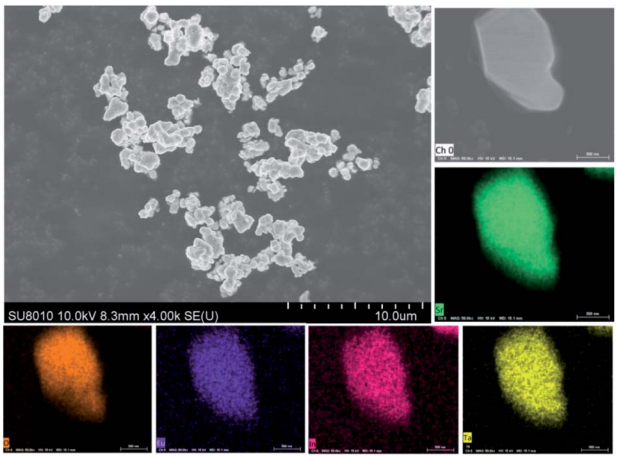

Fig. 3 The SEM diagrams of Sr_2InTaO_6:0.12Eu^{3+} phosphor and elemental mapping of the sample.

3.2 Electronic structure and optical band gap

In order to clarify the actual contribution on the photophysical properties of Sr_2InTaO_6, the first-principle theoretical calculations were carried out by the Vienna *Ab initio* Simulation Package (VASP).[30,31] As shown in Fig. 4(a), the calculated bandgap is indirect and the calculated value is 3.823 eV. The electronic band structure and the corresponding projected density of states (PDOS) of Sr_2InTaO_6 host material and Sr_2InTaO_6:0.12Eu^{3+} were presented in Fig. 4(b) and S1 (ESI†). Further analysis of PDOS shows that the eigenstates around

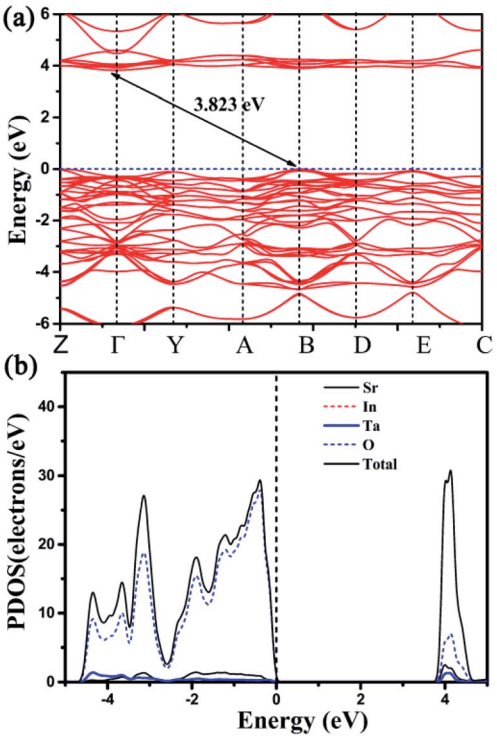

Fig. 4 (a) The calculated electronic band structure for host Sr_2InTaO_6. (b) The corresponding projected density of states of host Sr_2InTaO_6.

Fermi level (E_f) mainly attributes to the In and O atoms, whereas Sr and Ta atoms basically do not make contribution to the bands near E_f. This result indicates that the photophysical properties of Sr_2InTaO_6 are largely determined by the [InO_6] unit.

To verify the band gap experimentally, the DRS of Sr_2InTaO_6 host material and Sr_2InTaO_6:xEu^{3+} (x = 0.08, 0.12) samples are shown in Fig. 5. We can see that the samples show strong absorption in UV and NUV light region at about 260 nm to 350 nm. It can be ascribed to the charge-transfer band (CTB) of O^{2-} to Eu^{3+}, which is matching well with the excitation spectra.[32] Two little faintly visible drops located at 394 nm and 468 nm are aroused from the typical f–f electron transitions of the Eu^{3+} ion.[33] In summary, Sr_2InTaO_6:$0.12Eu^{3+}$ showed a wide absorption band at the NUV region which indicated that these materials had applicability in the WLEDs applications. The band gap of these samples can be computed by Kubelka–Munk means *via* below formula:[34]

$$F(R\infty h\nu)^n = A(h\nu - E_g) \quad (1)$$

$$F(R_\infty) = (1 - R)^2/2R = K/S \quad (2)$$

where $F(R_\infty)$ is Kubelka–Munk function, ν denotes the photon energy, h represents Plank constant, A is the proportionality coefficient, E_g denotes the bandgap value, and the index n depends on the type of energy transition. The values of n (2, 1/2, 3/2 or 3) are respectively for a direct transition, a indirect transition, a inhibitory direct transition and a inhibitory indirect transition.[35] The prepared fluorescent material is an indirect bandgap semiconductor as shown by previous theoretical calculation band gap value in Fig. 4. So n is equal to 1/2 in eqn (1). The value of E_g (~3.84 eV) can be gained from linear extrapolation of $[F(R_\infty)h\nu]^2 = 0$ (inset Fig. 5), which is usually a little bit bigger than that calculated value of Sr_2InTaO_6 host (~3.823 eV). And the plots for other n indexes are also shown in Fig. S2 (ESI),† It is attributed to the local density approximation (LDA), leading to an underestimate of the band gaps.[36]

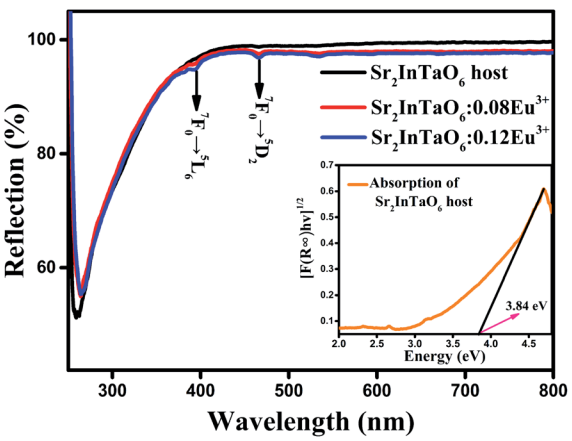

Fig. 5 Diffuse reflectance spectra of Sr_2InTaO_6:xEu^{3+} (x = 0, 0.08 and 0.12) samples. Inset: Absorption spectra of Sr_2InTaO_6 as calculated by the Kubelka–Munk function.

3.3 Detailed luminescence properties of Sr_2InTaO_6:Eu^{3+} phosphors

From the PLE spectra shown in Fig. 6(a), the first wide excitation peak from 200 to 300 nm with the largest value at approximately 246 nm is observed. It can be ascribed to the CTB from O^{2-} to Eu^{3+}. The other narrow excitation peaks centered at 363 nm, 384 nm, 394 nm, 417 nm, and 468 nm are respectively attributed to the characteristic 4f-4f transition ($^7F_0$–$^5D_4$, $^7F_0$–$^5L_7$, $^7F_0$–$^5L_6$, $^7F_0$–$^5D_3$ and $^7F_0$–$^5D_2$) of Eu^{3+}.[22,32] Moreover, the sharp excitation region at approximately 394 nm just yet located at the NUV region, confirming that the Sr_2InTaO_6:Eu^{3+} phosphors can be served as red fluorescent material. The PL spectra of Sr_2InTaO_6:xEu^{3+} with six doping concentrations (x = 0.04, 0.08, 0.12, 0.16, 0.20, 0.24) under 394 nm are shown in Fig. 6(b). Evidently, we can see that the shape and position of all samples exhibited similar emission profiles under different Eu^{3+} concentrations. At the excitation wavelength of 394 nm, the model exhibited a maximum emission at 624 nm, which is assigned to the $^5D_0 \rightarrow {}^7F_2$ conversion of Eu^{3+}.[24,33] Additionally, the Fig. 6(b) reflected the PL strength of the sample. It was observed that the emission intensity of Eu^{3+} ions increases with the doping contents (x) increasing and reaches a maximum at x = 0.12, then it begins to decrease monotonously for extra Eu^{3+} concentration. That is to say, this phosphor appeared concentration quenching phenomenon.

Concentration quenching effect is commonly ascribed to the energy transfer among the closest Eu^{3+}–Eu^{3+} ions. Generally speaking, there are three ways to explain energy transfers respectively are multipole–multipole interaction, exchange interaction, and radiation reabsorption.[37] To further investigate the concentration quenching effect among Eu^{3+} in Sr_2InTaO_6, the critical distance (R_c) between two activator ions (donor and acceptor) should be calculated to determine the way of energy transfer. The R_c was evaluated through this Blasse formula:[38]

$$R_c \approx 2\left[\frac{3V}{4\pi x_c N}\right]^{1/3} \quad (3)$$

where V refers to the volume of per crystal cell, χ_c represents the doped-Eu^{3+} critical concentration, N denotes the number of replaced Eu^{3+} ions each unit. In this case, the V = 268.103 Å^3, χ_c = 0.12 and N = 2, separately. Consequently, the analyzed R_c value of Eu^{3+} is to be about 12.86 Å, which is greater than 5 Å. This revealed that the mode of energy transfer is mainly from electric multipolar interaction instead of the exchange interaction and radiation reabsorption. For the further investigation, the electric multipolar interaction is composed of three types: dipole–dipole (d–d), quadrupole–quadrupole (q–q), and dipole–quadrupole (d–q).[39] Based on the theory of Dexter, to further confirm the type of electric multipolar interaction in Eu^{3+} ions, the equation as shown below is usually applied:[40]

$$\frac{I}{x} = K\left(1 + \beta(x)^{Q/3}\right)^{-1} \quad (4)$$

where I is emission intensity for Sr_2InTaO_6:Eu^{3+} phosphors, x denotes activator concentration; K is constant at identical excitation status. And Q = 6, 8, 10 separately represent the d–d,

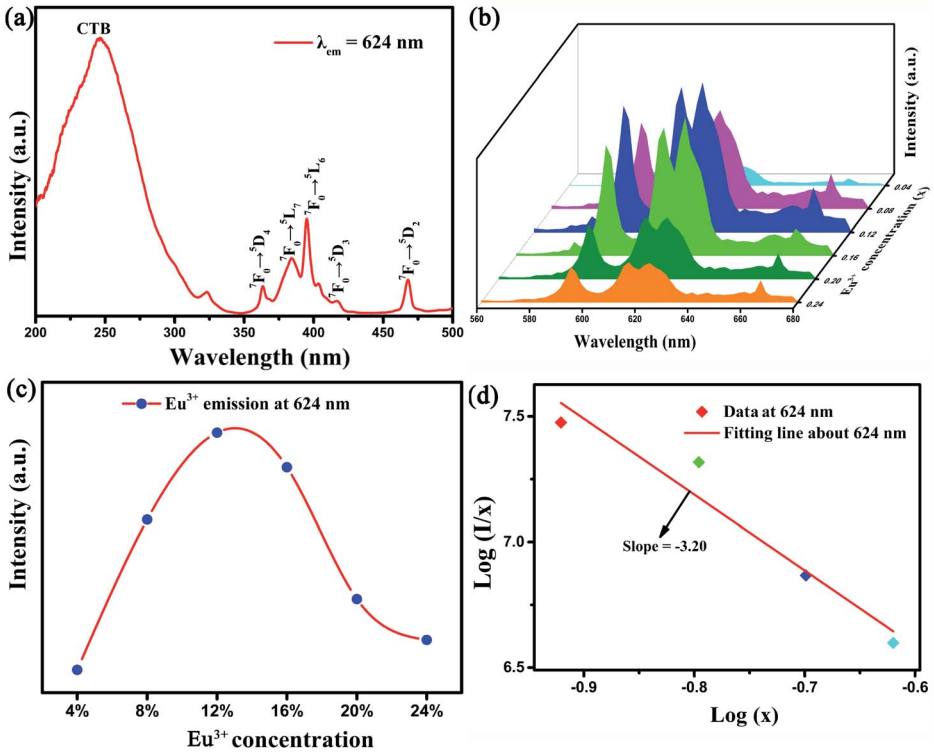

Fig. 6 (a) PLE of the Sr_2InTaO_6:0.12Eu^{3+} phosphor (b) PL of Sr_2InTaO_6:xEu^{3+} (x = 0.04, 0.08, 0.12, 0.16, 0.20, 0.24) samples. (c) The relationship of emission intensity and Eu^{3+} doping concentration. (d) Plot of log(I/x) *versus* log(x) for the 624 nm emission of Eu^{3+} ions in Sr_2InTaO_6 phosphors.

d–q and q–q interaction. Subsequent analysis, the value of Q can be gained by linear fitting with the correlation of log(x) and log(I/x), as depicted in Fig. 6(d). The detected slope is −3.20, then Q = 9.6. The value is close to 10, suggesting the q–q interaction takes major responsibility for concentration quenching effect among Sr_2InTaO_6:Eu^{3+} samples.

In order to further analyze the characteristics of fluorescence lifetime, as plotted in Fig. 7, the relaxation time at 624 nm of Sr_2InTaO_6:xEu^{3+} phosphors (x = 0.04, 0.08, 0.12, 0.16, 0.20, 0.24) under excitation 394 nm were carried out to research the luminescence dynamics. All decay curves are nicely matched with the double-exponential formula:[41]

$$I(t) = A_1 \exp(-t/t_1) + A_2 \exp(-t/t_2) \quad (5)$$

where I denotes the luminescence strength, A_1 and A_2 refer to constants, τ_1 and τ_2 stand for the short and long lifetimes of exponential parts. Based on the fitting result shown in Table 2, the lifetime was calculated to be 1.071, 0.970, 0.959, 0.926 and 0.919 ms following Eu^{3+} doping ratio 0.04, 0.08, 0.12, 0.16 and 0.20, respectively. This result showed that the decay time declined from 1.071 to 0.919 ms as the Eu^{3+} concentrations ascend which demonstrated by the nonradioactive energy transfer among Eu^{3+}.[42] The quantum efficiency (QE) of the Sr_2InTaO_6:0.12Eu^{3+} sample measured at room temperature under

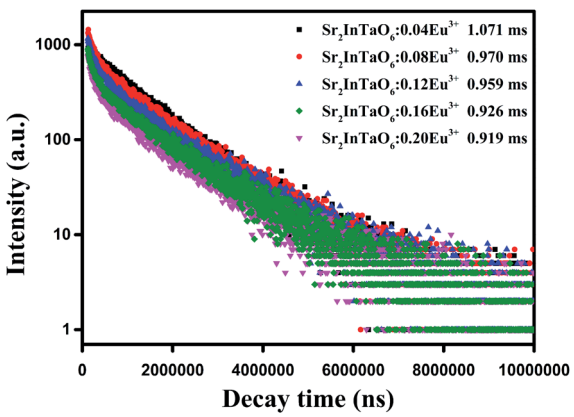

Fig. 7 The decay curves and calculated lifetimes of Sr_2InTaO_6:xEu^{3+} samples under 394 nm excitation and monitored at 624 nm.

Table 2 CIE chromaticity coordinates, color purity, and lifetimes of Sr_2InTaO_6:xEu^{3+} phosphors (0.04 ≤ x ≤ 0.24)

Sr_2InTaO_6:xEu^{3+}	x	y	Lifetime (ms)	Color purity (%)
Sr_2InTaO_6:0.04Eu^{3+}	0.6213	0.3741	1.071	93.8
Sr_2InTaO_6:0.08Eu^{3+}	0.6226	0.3729	0.970	96.1
Sr_2InTaO_6:0.12Eu^{3+}	0.6265	0.3693	0.959	96.4
Sr_2InTaO_6:0.16Eu^{3+}	0.6190	0.3761	0.926	95.7
Sr_2InTaO_6:0.20Eu^{3+}	0.6177	0.3773	0.919	96.0
Sr_2InTaO_6:0.24Eu^{3+}	0.6213	0.3741	1.071	93.8

excitation at 394 nm was presented in Fig. S3 (ESI),† and the enlarged profile of the PL spectrum shown in the inset. The internal QE for the as-prepared sample is up to 58.4%, which is higher than that reported for several Eu^{3+} doped oxide phosphors in the recent years, such as $K_4BaSi_3O_9$:Eu^{3+} (QE: 27%), $Na_3Sc_2(PO_4)_3$:Eu^{3+} (QE: 49%) and approaches the commercial standards for phosphor.[43,44] The high QE value implies that Sr_2InTaO_6:Eu^{3+} is a promising phosphor material for application in WLEDs.

Further study, the other important index to evaluate phosphor is the thermal stability. The temperature-dependent emission spectra of Sr_2InTaO_6:0.12Eu^{3+} samples were analyzed and shown in Fig. 8(a). It can be observed that the coordinate of emission peaks basically remained unchanged, but the emission strength gradually declined with the increment of temperature ranging from 298 to 573 K. This can be ascribed to the striking thermal quenching effect. Fig. 8(b) shows the trend about the normalized temperature-dependent emission intensity more clearly. It can be seen that the luminous intensity at 423 K decreased to 66.4% of the value at 298 K. Also, upon cooling the temperature from 573 to 298 K, the luminescence intensity at 423 K remained about 64.2% of that at the initial temperature, as presented in Fig. S4 (ESI).† These results demonstrate the prepared phosphors have good heat resistance.

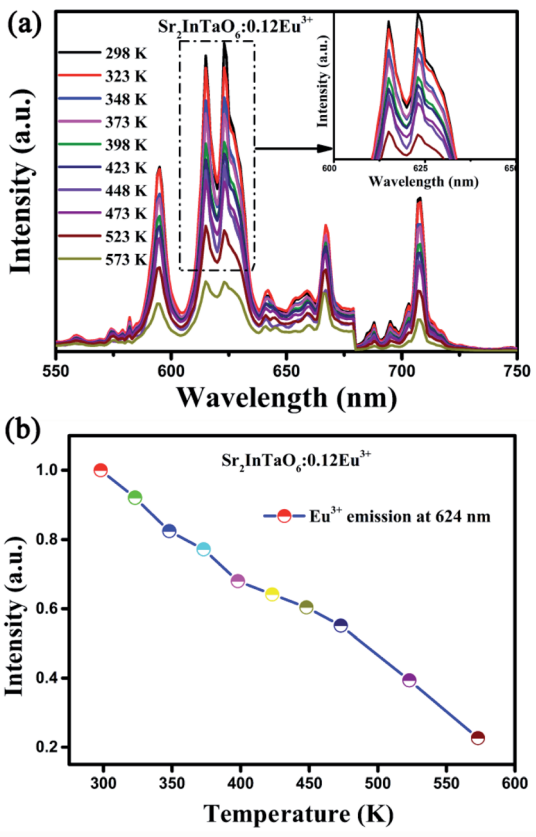

Fig. 8 (a) Temperature-dependent emission spectra of Sr_2InTaO_6:0.12Eu^{3+} samples. (b) Normalized emission intensity of Sr_2InTaO_6:0.12Eu^{3+} phosphors at different temperatures from 298 to 573 K.

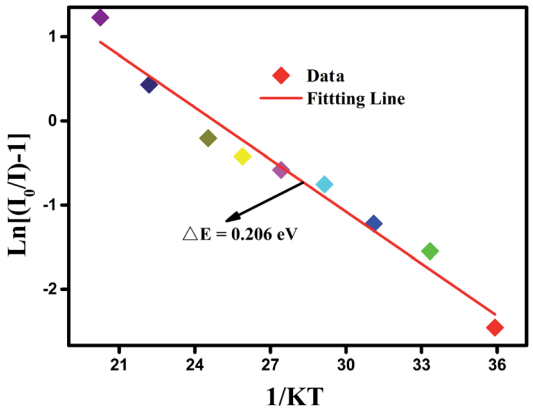

Fig. 9 The plot of $\ln(I_0/I - 1)$ *versus* $1/kT$ at the corresponding temperature.

Remarkably, the reason of thermal quenching can be explained from two aspects. One is notably ascribed to the nonradioactive transition from the excited states to ground state. The other one is the thermal excited ionization effect from 5d orbits to the charge band.[45] To better understand the reduced luminous intensity, the activation energy (ΔE) as performed to illustrate the thermal quenching effect as shown in Fig. 9. The following Arrhenius formula is adopted to calculate the ΔE of thermal quenching:[46]

$$\ln\left(\frac{I_0}{I} - 1\right) = \ln A - \frac{\Delta E}{kT} \quad (6)$$

where I_0 represents the emission strength at initial temperature, I denotes the strength at operated temperature T, k represents Boltzmann's constant with value of 8.69×10^5 eV K^{-1}, ΔE refers to the activation energy. From Fig. 9, the correlation between ln $[(I_0/I) - 1]$ and $1/kT$ was well linear matched with a slope factor of -0.206, so the ΔE for the thermal quenching equals to 0.206 eV. The comparatively higher ΔE proved that the prepared materials had good thermal stability.

The color-coordinate is another important index to evaluate the performance of fluorescent materials. Therefore, according to the PL spectra, the Commission Internationale de L'Eclairage (CIE) coordinate for Eu^{3+}-doped Sr_2InTaO_6 was calculated and shown in Table 2. As shown in Fig. 10, the CIE coordinates of the Sr_2InTaO_6:0.12Eu^{3+} phosphor is (0.6265, 0.3693), which are closed to the standard red chromaticity (0.67, 0.33) of National Television Standard Committee (NTSC) system.[47] When illuminated with the 365 nm UV lamp, the prepared samples showed efficient red color (as shown inset). It revealed that the red-emitting phosphor Sr_2InTaO_6:Eu^{3+} is a potential candidate for display in WLEDs. Moreover, the coordinates are at the edge of the CIE diagram, demonstrating that the phosphors show good color purity. The color purity can be estimated on the basis of the following equation:[48]

$$\text{Color purity} = \sqrt{\frac{(x_s - x_i)^2 + (y_s - y_i)^2}{(x_d - x_i)^2 + (y_d - y_i)^2}} \quad (7)$$

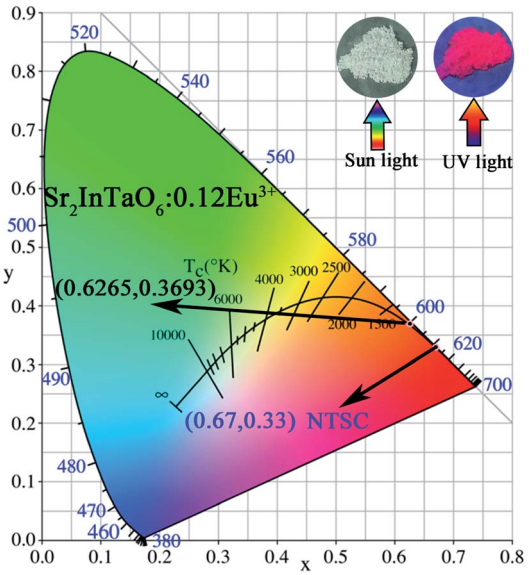

Fig. 10 CIE chromaticity coordinates diagram of Sr_2InTaO_6:0.12Eu^{3+} phosphors.

where x_s and y_s denote the color coordinates; x_i and y_i are the illuminant point of the 1931 CIE Standard Source C; x_d and y_d refer to color coordinates of the dominant wavelength. In this work, the (x_s, y_s), (x_i, y_i), and (x_d, y_d) are (0.6265, 0.3693), (0.310, 0.316), and (0.6322, 0.3767), respectively. The color purity of the Sr_2InTaO_6:0.12Eu^{3+} phosphors is 96.4%, which indicates that the Eu^{3+}-activated Sr_2InTaO_6 samples have good CIE chromaticity coordinate and high color purity.

4. Conclusions

In Summary, series of Eu^{3+}-doped Sr_2InTaO_6 double perovskite red phosphors were successfully obtained by solid state reaction method. The XRD, Rietveld refinement and SEM were executed to confirm the crystal structure and morphology information. Optical energy band gap of the host material Sr_2InTaO_6 was calculated by first-principles DFT with the VASP, which was consistent with the result of DRS. The PL, PLE and temperature-related emission spectra were systematically investigated to explain the advantage of doping Eu^{3+} ion. The optimal doping concentration value of Sr_2InTaO_6:$x$$Eu^{3+}$ is about 0.12 and the cause of concentration quenching can be ascribed to the q–q interaction. The decay curves of Sr_2InTaO_6:$x$$Eu^{3+}$ phosphors monitored at 394 nm were both displayed double exponential behavior and the lifetimes decreased from 1.071 to 0.919 ms with the increase of the Eu^{3+} doping concentration. Subsequently, temperature-dependent luminescence intensity spectra of Sr_2InTaO_6:0.12Eu^{3+} were also executed, in which the luminescence intensity reduced to 66.4% at 423 K and thus confirmed very good thermal stability. The mechanism of thermal quenching is explained from the non-radiative transition. In summary, the results indicated that Sr_2InTaO_6:Eu^{3+} phosphors have potential applications in the applications of WLEDs.

Conflicts of interest

There are no conflicts to declare.

Acknowledgements

This work was supported by National Natural Science Foundation of China (No. 21576002), Natural Science Foundation of Shandong Province, China (No. ZR2019PEM006), National College Students' Innovation and Entrepreneurship Training program (No. 201814276002).

Notes and references

1 P. Pattison, J. Tsao, G. Brainard and B. Bugbee, *Nature*, 2018, **563**, 493–500.
2 Z. G. Xia and Q. L. Liu, *Prog. Mater. Sci.*, 2016, **84**, 59–117.
3 K. Saidi and M. Dammak, *RSC Adv.*, 2020, **10**, 21867–21875.
4 E. F. Schubert and J. K. Kim, *Science*, 2005, **308**, 1274–1278.
5 P. Push, P. J. Schmidt and W. Schnick, *Nat. Mater.*, 2015, **14**, 454.
6 Z. Xia and A. Meijerink, *Chem. Soc. Rev.*, 2017, **46**, 275–299.
7 H. Guo, Z. G. Zheng, L. M. Teng, R. F. Wei and F. F. Hu, *J. Lumin.*, 2019, **213**, 494–503.
8 L. Wang, R. J. Xie, T. Suehiro, T. Takeda and N. Hirosaki, *Chem. Rev.*, 2018, **118**, 1951–2009.
9 F. W. Kang, G. H. Sun, P. Boutinaud, F. Gao, Z. H. Wang, J. Lu, Y. Y. Li and S. S. Xiao, *J. Mater. Chem. C*, 2019, **7**, 11041.
10 R. Kasuya, T. Isobe and H. Kuma, *J. Alloys Compd.*, 2006, **408**, 820–823.
11 Q. Li, L. Gao and D. Yan, *Mater. Chem. Phys.*, 2000, **64**, 41–44.
12 D. J. Liu, X. H. Yun, G. G. Li, P. P. Dang, M. S. Molokeev, H. Z. Lian, M. M. Shang and J. Lin, *Adv. Opt. Mater.*, 2020, 2001037.
13 Z. F. Yang, C. J. Ji, G. N. Zhang, G. M. Han, H. Wang, H. X. Bu, X. Tan, D. H. Xu and J. Y. Sun, *J. Lumin.*, 2019, **206**, 585–592.
14 X. X. Ma, L. B. Liao, Q. F. Guo, H. K. Liu, D. Yang, N. Liu and L. F. Mei, *RSC Adv.*, 2019, **9**, 35717–35726.
15 P. Q. Cai, L. Qin, C. L. Chen, J. Wang, S. Bi, S. I. Kim, Y. L. Huang and H. J. Seo, *Inorg. Chem.*, 2018, **57**, 3073–3081.
16 D. P. Cui, Z. Song, Z. G. Xia and Q. L. Liu, *J. Lumin.*, 2018, **199**, 271–277.
17 D. J. Liu, X. H. Yun, P. P. Dang, H. Z. Lian, M. M. Shang, G. G. Li and J. Lin, *Chem. Mater.*, 2020, **32**, 3065–3077.
18 A. J. Fu, A. X. Guan, F. F. Gao, X. S. Zhang, L. Y. Zhou, Y. B. Meng and H. M. Pan, *Opt. Laser Technol.*, 2017, **96**, 43–49.
19 S. J. Mofokeng, L. L. Noto and M. S. Dhlamini, *J. Lumin.*, 2020, **228**, 117569.
20 C. Yue, D. C. Zhu, Q. Yan and Y. Pu, *RSC Adv.*, 2020, **9**, 26364–26372.
21 K. Uematsu, A. Ochiai and K. Toda, *J. Alloys Compd.*, 2006, **408**, 860–863.
22 J. K. Han, G. A. Hirata and J. B. Talbot, *Mater. Sci. Eng.*, 2011, **176**, 436–441.
23 S. Ekambaram, K. C. Patil and M. Maaza, *J. Alloys Compd.*, 2005, **393**, 81–92.

24 C. R. Garcia, J. Oliva and G. A. Hirata, *Ceram. Int.*, 2017, **43**, 12876.
25 S. C. Lal, V. Lalan and G. Subodh, *Inorg. Chem.*, 2018, **57**, 6226–6236.
26 F. X. Liu, Y. Z. Fang, J. S. Hou, N. Zhang and Z. F. Ma, *Ceram. Int.*, 2014, **40**, 3237–3241.
27 R. D. Shannon, *Acta Crystallogr.*, 1976, **32**, 751–767.
28 A. R. Sharits, J. F. Khoury and P. M. Woodward, *Inorg. Chem.*, 2016, **55**, 12383–12390.
29 Y. Hua, W. Ran and J. S. Yu, *J. Alloys Compd.*, 2020, **835**, 155389.
30 Z. F. Yang, L. L. Yang, C. J. Ji, D. H. Xu, C. Q. Zhang, H. X. Bu, X. Tan, X. Y. Yun and J. Y. Sun, *J. Alloys Compd.*, 2019, **802**, 628–635.
31 D. Y. Huang, P. P. Dang, Y. Wei, B. Bai, H. Z. Lian, Q. G. Zeng and J. Lin, *Mater. Res. Bull.*, 2020, **124**, 110743.
32 P. P. Du, Q. H. Meng, X. J. Wang, Q. Zhu, X. D. Li, X. D. Sun and J. G. Li, *Chem. Eng. J.*, 2019, **375**, 121937.
33 Z. Jia, X. L. Zhang, X. Y. Hua, Y. Dong, H. L. Li, C. Q. Feng, Y. G. Wang and M. J. Xia, *J. Alloys Compd.*, 2020, **844**, 155875.
34 W. Soller, *Phys. Rev.*, 1924, **24**, 158–167.
35 Z. G. Xia, Z. H. Xu, M. Y. Chen and Q. L. Liu, *Dalton Trans.*, 2016, **45**, 11214–11232.
36 G. B. Nair, H. C. Swart and S. J. Dhoble, *Prog. Mater. Sci.*, 2020, **109**, 100622.
37 M. F. Joubert, A. Remillieux, B. Jacquier, J. Mugnier, B. Boulard, O. Perrot and C. Jacoboni, *J. Non-Cryst. Solids*, 1995, **184**, 341–345.
38 G. Blasse, *J. Solid State Chem.*, 1986, **62**, 207–211.
39 Z. F. Yang, D. H. Xu, J. N. Du, X. D. Gao and J. Y. Sun, *RSC Adv.*, 2016, **6**, 87493–87501.
40 D. L. Dexter and J. H. Schulman, *J. Chem. Phys.*, 1954, **22**, 1063.
41 C. Wei, D. H. Xu, J. Li, A. C. Geng, X. Li and J. Y. Sun, *J. Mater. Sci.: Mater. Electron.*, 2019, **30**, 2864–2871.
42 X. Geng, Y. Xie, Y. Y. Ma, Y. Y. Liu, J. M. Luo, J. X. Wang, R. J. Yu, B. Deng and W. M. Zhou, *J. Alloys Compd.*, 2020, **847**, 156249.
43 D. Stefanska, M. Stefa nski and P. J. Deren, *Opt. Mater.*, 2014, **37**, 410–413.
44 H. Guo, X. Huang and Y. Zeng, *J. Alloys Compd.*, 2018, **741**, 300–306.
45 J. Y. Sun and D. P. Cui, *J. Am. Ceram. Soc.*, 2014, **97**, 843.
46 S. Bhushan and M. V. Chukichev, *J. Mater. Sci. Lett.*, 1988, **9**, 319–321.
47 S. J. Wang, C. C. Xu and X. B. Qiao, *Ceram. Int.*, 2020, **47**, 1063–1075.
48 H. Guo, X. Huang and Y. Zeng, *J. Alloys Compd.*, 2018, **741**, 300–306.